Synthesis and polymorph manipulation of $FeSe_2$ monolayers

Zehao He[1,2,3*], Shiva Prasad Poudel[4*], Samuel Stolz[1*], Tiancong Zhu[1,2*], Tianye Wang[1,2], Antonio Rossi[5], Feng Wang[1,2,6], Sung-Kwan Mo[7], Alexander Weber-Bargioni[5], Zi Qiang Qiu[1,2], Salvador Barraza-Lopez[4], and Michael F. Crommie[1,2,6]

[1]*Department of Physics, University of California, Berkeley, CA 94720, USA.*

[2]*Materials Sciences Division, Lawrence Berkeley National Laboratory, Berkeley, CA 94720, USA.*

[3]*Department of Material Science and Engineering, University of California, Berkeley, CA 94720, USA.*

[4]*Department of Physics, University of Arkansas, Fayetteville, Arkansas 72701, USA and MonArk NSF Quantum Foundry, University of Arkansas, Fayetteville, Arkansas 72701, USA.*

[5]*The Molecular Foundry, Lawrence Berkeley National Laboratory, Berkeley, California 94720, USA.*

[6]*Kavli Energy NanoScience Institute at the University of California, Berkeley and the Lawrence Berkeley National Laboratory, Berkeley, CA 94720, USA.*

[7]*Advanced Light Source, Lawrence Berkeley National Laboratory, Berkeley, CA 94720, USA.*

Corresponding author e-mail address: crommie@berkeley.edu

Abstract

Polymorph engineering involves the manipulation of material properties through a controlled structural modification and is a candidate technique for creating unique 2D transition metal dichalcogenide (TMDC) nanodevices. Despite its promise, polymorph engineering of *magnetic* TMDC monolayers has not yet been demonstrated. Here we grow $FeSe_2$ monolayers via molecular beam epitaxy (MBE) and find that they have great promise for magnetic polymorph engineering. Using scanning tunneling microscopy (STM) and spectroscopy (STS) we find that $FeSe_2$ monolayers predominantly display a 1T' structural polymorph at 5 K. Application of voltage pulses from an STM tip causes a local, reversible transition from the 1T' phase to the 1T phase. Density functional theory (DFT) calculations suggest that this single-layer structural phase transition is accompanied by a magnetic transition from an antiferromagnetic to a ferromagnetic configuration. Those results open new possibilities for creating functional magnetic devices with TMDC monolayers via polymorph engineering.

Keywords

Polymorphism, magnetism, two-dimensional materials, scanning tunneling microscopy, phase transitions, density-functional theory

TMDC monolayers have demonstrated great potential for next-generation electronic, magnetic, and optical applications.[1] These atomically-thin materials host a variety of novel phenomena including non-trivial topology,[2–4] superconductivity,[5,6] charge density waves,[5,7–9] magnetism,[10,11] and Mott insulating phases[6,12,13], most of which are highly tunable through electrostatic gating and strain.[14–18] The coexistence of different crystal structures having the same stoichiometry in TMDC monolayers provides unique opportunities for TMDC polymorph engineering. The three main polymorphs for TMDC monolayers are the trigonal prismatic (1H), the octahedral (1T), and the distorted octahedral (1T') lattices, each of which exhibits very different physical properties. Structural manipulation between TMDC monolayer polymorphs has been used to induce topological transitions between the 1T' and 1H phases in WSe_2 and $MoTe_2$,[19,20] as well as metal-insulator transitions between the 1H and 1T phases of $TaSe_2$, TaS_2, and $NbSe_2$.[21–23] Polymorph engineering of TMDC monolayers has been achieved through temperature,[24] strain,[14] charge doping,[15,16] laser irradiation,[25] and by applying local electric fields,[21–23,26] thus expanding the toolbox for creating functional devices based on TMDC monolayers. Despite rapid progress in experimentally controlling polymorphism in TMDC monolayers, however, the manipulation of magnetism in these materials through polymorph engineering is still in its infancy, mainly due to a lack of suitable material platforms.

Here we demonstrate that monolayer $FeSe_2$ is a promising candidate for magnetic polymorph engineering through a combined experimental and theoretical investigation. The $FeSe_2$ monolayers used in this study were grown *via* molecular beam epitaxy (MBE). STM investigation reveals that our $FeSe_2$ monolayers occur mainly in a stripe phase that we identify as the 1T'-polymorph. We find that $FeSe_2$ monolayers can be locally converted into a hexagonal phase that we identify as the 1T-$FeSe_2$ polymorph upon application of voltage pulses from the STM tip. This phase transition can be reversed by heating the sample above 50 K, thus establishing the 1T'-polymorph as the ground state structure. DFT+U calculations confirm

the assignment of 1T' and 1T polymorphs to the stripe and hexagonal phases and corroborate that 1T'-$FeSe_2$ is the most stable polymorph and that it has a low energy barrier for structural phase transitions. Our calculations further suggest the existence of antiferromagnetic order in monolayer 1T'-$FeSe_2$ and ferromagnetic order in the monolayer 1T-$FeSe_2$ phase over a large range of values for the parameter U.

$FeSe_2$ monolayers were grown on highly oriented pyrolytic graphite (HOPG) using MBE under a Se-rich environment (see methods for growth details). The growth was monitored using reflection high-energy electron diffraction (RHEED) as shown in Fig. 1a. We observe concurrent growth of FeSe and $FeSe_2$ monolayers. During growth at 800 K the RHEED intensity from $FeSe_2$ monolayer (red lines in Fig. 1a) is stronger than monolayer FeSe intensity (green lines in Fig. 1a). Upon cool-down to 300 K the relative RHEED intensity of monolayer FeSe increases, indicating that monolayer $FeSe_2$ is a metastable phase.

Low temperature (5 K) STM and STS measurements were performed to gain insight into the structural and electronic properties of monolayer $FeSe_2$. The large-scale STM image shown in Fig. 1b depicts monolayer $FeSe_2$ islands on HOPG that have a step height of about 8.2 ± 0.2 Å. The high-resolution STM images and STS data shown in Figs. 1c - f enable us to differentiate the structure and density of states of monolayer FeSe *versus* monolayer $FeSe_2$. Monolayer FeSe (Fig. 1c) is observed to have a square unit cell with lattice constant 3.8 Å ± 0.1 Å, as seen previously[27]. Our STS spectra obtained from monolayer FeSe (Fig. 1f, green curve) is also in agreement with previous STS measurements[27]. All non-FeSe monolayer islands are identified as $FeSe_2$ and are observed to have two different polymorphs. The majority of $FeSe_2$ monolayer islands show a stripe phase (Fig. 1d), accounting for more than 90% of total $FeSe_2$ island area. An atomically resolved image of the stripe phase reveals a rectangular unit cell with lattice constants 3.9 Å ± 0.1 Å, 6.7 Å ± 0.1 Å (Fig. 1d, bottom panel). The atomic structure and symmetry of the stripe phase is similar to previous observations of 1T'-WTe_2[4]

(although a slight period-doubling in the long direction can be seen for $FeSe_2$ (see Supplementary Fig. 1)). The remaining fraction of the $FeSe_2$ monolayer islands exhibit a hexagonal phase with lattice constant 3.8 Å ± 0.1 Å (Fig. 1e) that is consistent with either the 1T or the 1H TMDC polymorphs. STS measurements shown in the inset to Fig. 1f reveal that both phases of monolayer $FeSe_2$ exhibit a non-vanishing dI/dV signal near the Fermi level, thus indicating metallic behavior.

Fig. 2 shows the process by which the stripe phase of monolayer $FeSe_2$ can be locally converted into the hexagonal phase by applying a voltage pulse from the STM tip. Fig. 2a shows an $FeSe_2$ island before tip pulsing where most of the island is in the stripe phase (see dashed line phase boundary). To induce a local phase change, the STM tip was positioned at the location indicated by the white cross in Fig. 2b and a voltage pulse of + 3.4 V was applied for 100 ms with the STM feedback loop open ($V_B = -1$ V, $I_T = 10$ pA for the tunnel set point). After the pulse the region near the tip-pulse position is seen to convert from the stripe phase to the hexagonal phase (see lower dashed line boundary). The close-up image in the inset to Fig. 2b shows the hexagonal symmetry of the converted region (this region has an area similar to the altered regions observed in other STM-driven phase transitions[21,28,29]). The rest of the island was converted from the stripe phase to the hexagonal phase by scanning the entire island with a bias voltage V_B = + 3.5 V ($I_T = 10$ pA) (Fig. 2c). Once converted to the hexagonal phase, the island could not be changed back to the stripe phase by pulsing despite applying numerous voltage pulses in the range $-5\text{ V} < V_{pulse} < +5\text{ V}$.

To better characterize the phase conversion process, we systematically determined the threshold pulse voltage required to convert different stripe-phase islands to the hexagonal phase. For each island a low voltage pulse of + 2 V was first applied (using the initial tunnel set point $V_B = -1$ V, $I_T = 10$ pA) and then incrementally higher pulses were applied up to a maximum of + 5 V (using the same initial set point) *until* a tip-induced structural phase

transition occurred. A histogram of the minimum voltage pulse required to cause local phase conversion at $T = 5$ K for different monolayer islands is plotted in Fig. 2d. Stripe phase islands that did not convert to the hexagonal phase after applying voltage pulses up to + 5 V are denoted "non-convertible" (NC). The phase conversion process is observed to be polarity-dependent, as no islands could be converted with negative pulses up to a magnitude of -4 V. At $T = 5$ K 98% of all monolayer islands in the stripe phase could be converted to the hexagonal phase using positive pulses (Fig. 2d) with the average threshold voltage being $\langle V_{th.} \rangle = 3.3$ V. No clear trend is seen regarding the area of the converted $FeSe_2$ region and the magnitude of the applied voltage pulse (see Supplementary Fig. 2). Possible mechanisms that might explain the 1T'-to-1T phase transition observed here include the effect of the tip-induced electric field on local electronic dipole moments[21,29], as well as the effect of electronic doping on the total energy of the 2D film[15,20].

The ease with which the stripe-to-hexagonal phase transition of $FeSe_2$ monolayers can be induced suggests a relatively low energy barrier between the stripe and hexagonal polymorphs. This implies that thermally-induced island structural transitions might be able to compete with tip-induced transitions at elevated temperatures. To test this hypothesis and gain insight into the magnitude of the relevant energy barrier, we performed additional experiments at higher temperatures using the switching protocol described above. Fig. 3a shows the tip-induced switching histogram for an ensemble of islands held at $T = 20$ K. The observed switching characteristics are very similar to those occurring at $T = 5$ K: all 23 islands were switched with $\langle V_{th.} \rangle = 3.1$ V. At higher temperatures, however, the switching behavior of the islands gradually changes. For example, Fig. 3b shows that at $T = 40$ K the threshold voltage raises to $\langle V_{th.} \rangle = 3.5$ V and 11% of the islands are non-convertible. At $T = 50$ K the threshold voltage increases to $\langle V_{th.} \rangle = 3.9$ V and 27% of the islands cannot switch (Fig. 3c). At $T = 60$ K the threshold voltage increases further to $\langle V_{th.} \rangle = 4.4$ V, while the non-switching fraction

jumps to 54% (Fig. 3d). The temperature-induced trend is seen in Fig. 3e which shows the non-switching fraction of islands as a function of temperature.

In addition to the apparent increased difficulty of switching with increased temperature, we also observe islands switching *back* to the stripe phase at higher temperatures. For example, at T = 20 K no islands return to the stripe phase for waiting times on the order of 1 minute while at T = 50 K we observe 25% of the islands switching back to the stripe phase after a 1 minute waiting period. The increased difficulty of the 1T'-to-1T phase transition with increased temperature is likely influenced by the increased rate of back conversions. This is consistent with the fact that the striped 1T' phase of monolayer $FeSe_2$ is the thermodynamically stable phase.

The temperature dependence of the switching behavior can be visualized for a single monolayer island as shown in Figs. 3f – i. Fig. 3f shows the entire island in the stripe phase at T = 50 K before switching (the dashed black line shows a grain boundary between two rotated 1T' domains (see SI section 3 for additional discussion of domain boundaries)). Fig. 3g shows the island after being pulsed at the marked location, causing the lower right quadrant to switch to the hexagonal phase (T = 50 K). The sample was then warmed to T = 60 K over a period of $\Delta t \sim$ 1 hour, whereupon the same island was reimaged. As shown in Fig. 3h, heating causes the island to switch back to the stripe phase with a grain boundary bisecting the island between two rotated 1T' domains (similar phase reversal also occurs for fully converted 1T islands as shown in SI section 4). This island could not be switched to the hexagonal phase via tip pulsing at T = 60 K, but the 1T'-1T' rotational grain boundary did shift as a result of pulsing (Fig. 3i) (similar tip-pulse-induced movement of 1T'-1T' grain boundaries has been seen in TMDC monolayers previously[26]).

To gain further insight into the properties of monolayer $FeSe_2$ we performed DFT calculations using the DFT+U method with U values ranging from 0 to 6 eV for the Fe *d*-orbital. As shown in Fig. 4a, our relaxed DFT structures systematically underestimate the lattice constants of the 1T' and 1T $FeSe_2$ polymorphs by about 9% compared to the STM data (the energetically unfavorable 1H polymorph has a lattice constant that is more than 18% smaller than the experimental hexagonal lattice constant). Slight underestimation of lattice constants is common for DFT-based methods.[30–33] Our DFT calculations provide useful insight into the energetics of the different $FeSe_2$ polymorphs, including their magnetic configurations. As shown in Fig. 4b, the 1T'-$FeSe_2$ monolayer is the energetically favorable polymorph for U $\leq$ 4 eV (more than 160 meV per formula unit (f.u.) lower in energy than 1H-$FeSe_2$) but is only ~ 5 meV per formula unit (f.u.) more stable than monolayer 1T-$FeSe_2$ for U = 4 eV. This leads to an energy difference of ~ 50 K between the 1T-$FeSe_2$ and 1T'-$FeSe_2$ phases, in reasonable agreement with the experimental results and supporting our choice of U = 4 eV.

Our DFT calculations provide insight into the magnetic ground states of the different polymorphs of monolayer $FeSe_2$. Fig. 4c shows that the 1T' rectangular AFM phase has the lowest energy of all the polymorph phases while the 1T FM phase is the nearest adjacent phase with an energy just 5 meV/f.u. higher (theoretically predicted magnetic orderings were seen to remain constant for electron and hole doping levels up to $10^{13}/cm^2$). No experimental signatures of inelastically-induced transitions between different theoretically predicted magnetic phases were observed for our $FeSe_2$ samples.

The magnetic moments of the 1T' rectangular AFM phase are predicted to have a magnitude of 3.59 μ_B per Fe atom and 0.09 μ_B per Se atom. The nearby 1T FM phase is predicted to have magnetic moments of 3.69 μ_B per Fe atom and 0.116 μ_B per Se atom (spin-polarized band structures for these magnetic configurations can be seen in Fig. 4e and are compared to experimental dI/dV spectra in Supplementary Fig. 6). The ferromagnetic 1T-$FeSe_2$

monolayer adopts an in-plane magnetic configuration with a magnetic anisotropy barrier of 1.1 meV per formula unit (Fig. 4d), consistent with an observed phase transition in magnetoresistance measured previously for multilayer 1T-$FeSe_2$ nanocrystals.[34]

The calculated magnetic states of both 1T-$FeSe_2$ and 1T'-$FeSe_2$ are consistent with each Fe atom transferring four electrons to surrounding Se atoms, thus changing the Fe electron shell structure from $4s^2 3d^6$ to $4s^0 3d^4$. The four remaining *d*-electrons are expected to result in 4 μ_B per Fe atom according to Hund's rule, which is reasonably consistent with our calculated magnetic moments. Because Fe atoms in $FeSe_2$ are next-nearest neighbors, the magnetic exchange interaction is likely dominated by super-exchange coupling through Se atoms, whose sign and magnitude can strongly depend on bond length and bond angles. This is the probable cause of the different magnetic ground states between monolayer 1T-$FeSe_2$ and monolayer 1T'-$FeSe_2$.

In conclusion, we have experimentally demonstrated growth of the 1T' polymorph of monolayer $FeSe_2$, as well as reversible manipulation between monolayer $FeSe_2$ 1T'- and 1T-polymorphs. The 1T'-$FeSe_2$ to 1T-$FeSe_2$ transition is realized electrically by applying a voltage pulse with the STM tip, while the 1T-$FeSe_2$ to 1T'-$FeSe_2$ transition is produced thermally. DFT simulations suggest that this structural phase transition is accompanied by a change from antiferromagnetic ordering in monolayer 1T'-$FeSe_2$ to ferromagnetic ordering in monolayer 1T-$FeSe_2$. The predicted difference in magnetic ordering between the 1T and 1T' phases combined with the experimentally observed reversible structural phase transition suggests that the magnetic ground state of $FeSe_2$ monolayers may be locally manipulated through their structural polymorph. $FeSe_2$ monolayers thus potentially provide a new platform for the investigation and manipulation of structural and magnetic phase transitions in the atomically thin limit.

Methods

MBE growth

Monolayer $FeSe_2$ samples were grown on highly-oriented pyrolytic graphite (HOPG) or on bilayer graphene on SiC(0001) substrates using molecular beam epitaxy. Before growth the substrates were cleaned by annealing them at 900 K overnight under ultra-high vacuum conditions with a pressure better than 2×10^{-10} mbar. Iron (Purity: 99.995%, SPIE) and selenium (Purity: 99.999%, Alfa Aesar) were then sublimated from an e-beam evaporator (flux: 0.08 Å/min) and a home-built Knudsen cell (flux: 8 Å/min) respectively until the desired surface coverage was achieved while holding the sample at 800 K.

STM measurements

Clean transfer of the sample from the MBE chamber to the STM chamber was achieved by capping the sample with 20 nm of amorphous Se to prevent degradation in air. Before STM measurement the samples were annealed in UHV at ~200 °C for 1 h to remove the Se capping layer and then transferred *in-situ* to the low temperature (T = 5 K) STM stage. Some samples were directly transferred from the MBE chamber to the STM chamber through a UHV suitcase to confirm the quality of the Se-capped samples.

STM measurements were performed in a low-temperature CreaTec UHV STM operated at a pressure below 2×10^{-10} mbar (T = 5 K for all STM measurements except where otherwise specified). Electrochemically etched tungsten tips were calibrated on a Cu(111) surface before performing other STM measurements. STS measurements were performed using standard lock-in techniques (frequency = 401 Hz). The STM tip was grounded during these measurements and bias voltages refer to the sample voltage.

To determine the lattice constants of epitaxial $FeSe_2$ monolayers we first calibrated our STM by obtaining atomic resolution of the underlying HOPG or graphene substrate. The STM

set point before applying voltage pulses for monolayer phase switching was typically $V_B = -1$ V, $I_T = 10$ pA. Voltage pulses of + 2 V were first applied and then increased by + 0.1 V until the stripe-to-hexagonal phase transition was observed via STM topography scans.

Computational methods

Electronic structure calculations were performed using density-functional theory as implemented in the VASP package[35]. PAW[36] pseudopotentials were used to describe the ionic potential of all atoms. We employed exchange-correlation functionals with self-consistent van der Waals corrections[37] using the optPBE-vdW functional.[38–40] A 30 x 15 x 1 k-point grid and cutoff energy of 500 eV were employed. Energy and force convergence criteria were set to 10^{-10} eV and 10^{-6} eV/Å, respectively. The out-of-plane lattice vector was set to 30 Å. A U-parameter was added to constrain the spatial extent of the Fe *d*-orbitals, which are often too extended in standard DFT. This approach also helps to provide more accurate magnetic exchange couplings. We applied DFT+U corrections[41,42] using the method by Dudarev *et al.*[43].

Acknowledgements

This research was supported by the Director, Office of Science, Office of Basic Energy Sciences, Materials Sciences and Engineering Division of the US Department of Energy, under contract number DE-AC02-05CH11231 within the van der Waals Heterostructures program (KCWF16) (STM/STS measurements). Support was also provided by the Center for Novel Pathways to Quantum Coherence in Materials, an Energy Frontier Research Center funded by the US Department of Energy, Office of Science, Basic Energy Sciences (MBE growth and characterization) and the National Science Foundation under grant DMR-2221750 (phase switching analysis). S.S. acknowledges Fellowship support by the Swiss National Science Foundation under project no.195133. S.P.P. and S.B.L. were supported by the National Science Foundation Q-AMASE-i program under grant DMR-1906383 (magnetic structure

simulations). DFT calculations were performed at the Pinnacle Supercomputer, funded by NSF under award OAC-2346752.

Data availability

The data presented in the paper is available under request.

Ethics declaration

The authors declare no competing interests.

Supporting Information

The supporting information contains Section 1: Atomic structure of monolayer $FeSe_2$ stripe phase; Section 2: Statistics for converted area versus magnitude of voltage pulses; Section 3: Additional experimental data on domain walls; Section 4: Phase reversal for a fully converted 1T island and Section 5: Experimental dI/dV spectra and calculated density of states (DOS).

References

(1) Manzeli, S.; Ovchinnikov, D.; Pasquier, D.; Yazyev, O. V.; Kis, A. 2D Transition Metal Dichalcogenides. *Nat. Rev. Mater.* **2017**, *2* (8), 1–15. https://doi.org/10.1038/natrevmats.2017.33.

(2) Fei, Z.; Palomaki, T.; Wu, S.; Zhao, W.; Cai, X.; Sun, B.; Nguyen, P.; Finney, J.; Xu, X.; Cobden, D. H. Edge Conduction in Monolayer WTe_2. *Nat. Phys.* **2017**, *13* (7), 677–682. https://doi.org/10.1038/nphys4091.

(3) Wu, S.; Fatemi, V.; Gibson, Q. D.; Watanabe, K.; Taniguchi, T.; Cava, R. J.; Jarillo-Herrero, P. Observation of the Quantum Spin Hall Effect up to 100 Kelvin in a Monolayer Crystal. *Science* **2018**, *359* (6371), 76–79. https://doi.org/10.1126/science.aan6003.

(4) Tang, S.; Zhang, C.; Wong, D.; Pedramrazi, Z.; Tsai, H.-Z.; Jia, C.; Moritz, B.; Claassen, M.; Ryu, H.; Kahn, S.; Jiang, J.; Yan, H.; Hashimoto, M.; Lu, D.; Moore, R. G.; Hwang, C.-C.; Hwang, C.; Hussain, Z.; Chen, Y.; Ugeda, M. M.; Liu, Z.; Xie, X.; Devereaux, T. P.; Crommie, M. F.; Mo, S.-K.; Shen, Z.-X. Quantum Spin Hall State in Monolayer 1T'-WTe_2. *Nat. Phys.* **2017**, *13* (7), 683–687. https://doi.org/10.1038/nphys4174.

(5) Ugeda, M. M.; Bradley, A. J.; Zhang, Y.; Onishi, S.; Chen, Y.; Ruan, W.; Ojeda-Aristizabal, C.; Ryu, H.; Edmonds, M. T.; Tsai, H.-Z.; Riss, A.; Mo, S.-K.; Lee, D.; Zettl, A.; Hussain, Z.; Shen, Z.-X.; Crommie, M. F. Characterization of Collective Ground States in Single-Layer $NbSe_2$. *Nat. Phys.* **2016**, *12* (1), 92–97. https://doi.org/10.1038/nphys3527.

(6) Vaňo, V.; Amini, M.; Ganguli, S. C.; Chen, G.; Lado, J. L.; Kezilebieke, S.; Liljeroth, P. Artificial Heavy Fermions in a van Der Waals Heterostructure. *Nature* **2021**, *599* (7886), 582–586. https://doi.org/10.1038/s41586-021-04021-0.

(7) Chen, P.; Chan, Y.-H.; Fang, X.-Y.; Zhang, Y.; Chou, M. Y.; Mo, S.-K.; Hussain, Z.; Fedorov, A.-V.; Chiang, T.-C. Charge Density Wave Transition in Single-Layer Titanium Diselenide. *Nat. Commun.* **2015**, *6* (1), 8943. https://doi.org/10.1038/ncomms9943.

(8) Feng, J.; Biswas, D.; Rajan, A.; Watson, M. D.; Mazzola, F.; Clark, O. J.; Underwood, K.; Marković, I.; McLaren, M.; Hunter, A.; Burn, D. M.; Duffy, L. B.; Barua, S.; Balakrishnan, G.; Bertran, F.; Le Fèvre, P.; Kim, T. K.; van der Laan, G.; Hesjedal, T.; Wahl, P.; King, P. D. C. Electronic Structure and Enhanced Charge-Density Wave Order of Monolayer VSe_2. *Nano Lett.* **2018**, *18* (7), 4493–4499. https://doi.org/10.1021/acs.nanolett.8b01649.

(9) Duvjir, G.; Choi, B. K.; Jang, I.; Ulstrup, S.; Kang, S.; Thi Ly, T.; Kim, S.; Choi, Y. H.; Jozwiak, C.; Bostwick, A.; Rotenberg, E.; Park, J.-G.; Sankar, R.; Kim, K.-S.; Kim, J.; Chang, Y. J. Emergence of a Metal–Insulator Transition and High-Temperature Charge-Density Waves in VSe_2 at the Monolayer Limit. *Nano Lett.* **2018**, *18* (9), 5432–5438. https://doi.org/10.1021/acs.nanolett.8b01764.

(10) O'Hara, D. J.; Zhu, T.; Trout, A. H.; Ahmed, A. S.; Luo, Y. K.; Lee, C. H.; Brenner, M. R.; Rajan, S.; Gupta, J. A.; McComb, D. W.; Kawakami, R. K. Room Temperature Intrinsic Ferromagnetism in Epitaxial Manganese Selenide Films in the Monolayer Limit. *Nano Lett.* **2018**, *18* (5), 3125–3131. https://doi.org/10.1021/acs.nanolett.8b00683.

(11) Zhang, X.; Lu, Q.; Liu, W.; Niu, W.; Sun, J.; Cook, J.; Vaninger, M.; Miceli, P. F.; Singh, D. J.; Lian, S.-W.; Chang, T.-R.; He, X.; Du, J.; He, L.; Zhang, R.; Bian, G.; Xu, Y. Room-Temperature Intrinsic Ferromagnetism in Epitaxial $CrTe_2$ Ultrathin Films. *Nat. Commun.* **2021**, *12* (1), 2492. https://doi.org/10.1038/s41467-021-22777-x.

(12) Nakata, Y.; Sugawara, K.; Shimizu, R.; Okada, Y.; Han, P.; Hitosugi, T.; Ueno, K.; Sato, T.; Takahashi, T. Monolayer 1T-$NbSe_2$ as a Mott Insulator. *NPG Asia Mater.* **2016**, *8* (11), e321–e321. https://doi.org/10.1038/am.2016.157.
(13) Chen, Y.; Ruan, W.; Wu, M.; Tang, S.; Ryu, H.; Tsai, H.-Z.; Lee, R.; Kahn, S.; Liou, F.; Jia, C.; Albertini, O. R.; Xiong, H.; Jia, T.; Liu, Z.; Sobota, J. A.; Liu, A. Y.; Moore, J. E.; Shen, Z.-X.; Louie, S. G.; Mo, S.-K.; Crommie, M. F. Strong Correlations and Orbital Texture in Single-Layer 1T-$TaSe_2$. *Nat. Phys.* **2020**, *16*, 218–224. https://doi.org/10.1038/s41567-019-0744-9.
(14) Song, S.; Keum, D. H.; Cho, S.; Perello, D.; Kim, Y.; Lee, Y. H. Room Temperature Semiconductor–Metal Transition of $MoTe_2$ Thin Films Engineered by Strain. *Nano Lett.* **2016**, *16* (1), 188–193. https://doi.org/10.1021/acs.nanolett.5b03481.
(15) Wang, Y.; Xiao, J.; Zhu, H.; Li, Y.; Alsaid, Y.; Fong, K. Y.; Zhou, Y.; Wang, S.; Shi, W.; Wang, Y.; Zettl, A.; Reed, E. J.; Zhang, X. Structural Phase Transition in Monolayer $MoTe_2$ Driven by Electrostatic Doping. *Nature* **2017**, *550* (7677), 487–491. https://doi.org/10.1038/nature24043.
(16) Zhu, X.; Li, D.; Liang, X.; Lu, W. D. Ionic Modulation and Ionic Coupling Effects in MoS_2 Devices for Neuromorphic Computing. *Nat. Mater.* **2019**, *18* (2), 141–148. https://doi.org/10.1038/s41563-018-0248-5.
(17) Maximenko, Y.; Chang, Y.; Chen, G.; Hirsbrunner, M. R.; Swiech, W.; Hughes, T. L.; Wagner, L. K.; Madhavan, V. Nanoscale Studies of Electric Field Effects on Monolayer 1T′-WTe_2. *Npj Quantum Mater.* **2022**, *7* (1), 1–6. https://doi.org/10.1038/s41535-022-00433-x.
(18) Zhu, T.; Ruan, W.; Wang, Y.-Q.; Tsai, H.-Z.; Wang, S.; Zhang, C.; Wang, T.; Liou, F.; Watanabe, K.; Taniguchi, T.; Neaton, J. B.; Weber-Bargioni, A.; Zettl, A.; Qiu, Z. Q.; Zhang, G.; Wang, F.; Moore, J. E.; Crommie, M. F. Imaging Gate-Tunable Tomonaga–Luttinger Liquids in 1H-$MoSe_2$ Mirror Twin Boundaries. *Nat. Mater.* **2022**, *21* (7), 748–753. https://doi.org/10.1038/s41563-022-01277-3.
(19) Duerloo, K.-A. N.; Li, Y.; Reed, E. J. Structural Phase Transitions in Two-Dimensional Mo- and W-Dichalcogenide Monolayers. *Nat. Commun.* **2014**, *5* (1), 4214. https://doi.org/10.1038/ncomms5214.
(20) Li, Y.; Duerloo, K.-A. N.; Wauson, K.; Reed, E. J. Structural Semiconductor-to-Semimetal Phase Transition in Two-Dimensional Materials Induced by Electrostatic Gating. *Nat. Commun.* **2016**, *7* (1), 10671. https://doi.org/10.1038/ncomms10671.
(21) Zhang, J.; Liu, J.; Huang, J. L.; Kim, P.; Lieber, C. M. Creation of Nanocrystals Through a Solid-Solid Phase Transition Induced by an STM Tip. *Science* **1996**, *274* (5288), 757–760. https://doi.org/10.1126/science.274.5288.757.
(22) Kim, J.-J.; Park, C.; Yamaguchi, W.; Shiino, O.; Kitazawa, K.; Hasegawa, T. Observation of a Phase Transition from the T Phase to the H Phase Induced by a STM Tip in 1T-TaS_2. *Phys. Rev. B* **1997**, *56* (24), R15573–R15576. https://doi.org/10.1103/PhysRevB.56.R15573.
(23) Bischoff, F.; Auwärter, W.; Barth, J. V.; Schiffrin, A.; Fuhrer, M.; Weber, B. Nanoscale Phase Engineering of Niobium Diselenide. *Chem. Mater.* **2017**, *29* (23), 9907–9914. https://doi.org/10.1021/acs.chemmater.7b03061.
(24) Zhang, F.; Wang, Z.; Dong, J.; Nie, A.; Xiang, J.; Zhu, W.; Liu, Z.; Tao, C. Atomic-Scale Observation of Reversible Thermally Driven Phase Transformation in 2D In_2Se_3. *ACS Nano* **2019**, *13* (7), 8004–8011. https://doi.org/10.1021/acsnano.9b02764.
(25) Cho, S.; Kim, S.; Kim, J. H.; Zhao, J.; Seok, J.; Keum, D. H.; Baik, J.; Choe, D.-H.; Chang, K. J.; Suenaga, K.; Kim, S. W.; Lee, Y. H.; Yang, H. Phase Patterning for Ohmic Homojunction Contact in $MoTe_2$. *Science* **2015**, *349* (6248), 625–628. https://doi.org/10.1126/science.aab3175.

(26) Pedramrazi, Z.; Herbig, C.; Pulkin, A.; Tang, S.; Phillips, M.; Wong, D.; Ryu, H.; Pizzochero, M.; Chen, Y.; Wang, F.; Mele, E. J.; Shen, Z.-X.; Mo, S.-K.; Yazyev, O. V.; Crommie, M. F. Manipulating Topological Domain Boundaries in the Single-Layer Quantum Spin Hall Insulator 1T′−WSe_2. *Nano Lett.* **2019**, *19*, 5634–5639. https://doi.org/10.1021/acs.nanolett.9b02157.

(27) Song, C.-L.; Wang, Y.-L.; Jiang, Y.-P.; Li, Z.; Wang, L.; He, K.; Chen, X.; Ma, X.-C.; Xue, Q.-K. Molecular-Beam Epitaxy and Robust Superconductivity of Stoichiometric FeSe Crystalline Films on Bilayer Graphene. *Phys. Rev. B* **2011**, *84* (2), 020503. https://doi.org/10.1103/PhysRevB.84.020503.

(28) Lee, J.; Wong, D.; Velasco Jr, J.; Rodriguez-Nieva, J. F.; Kahn, S.; Tsai, H.-Z.; Taniguchi, T.; Watanabe, K.; Zettl, A.; Wang, F.; Levitov, L. S.; Crommie, M. F. Imaging Electrostatically Confined Dirac Fermions in Graphene Quantum Dots. *Nat. Phys.* **2016**, *12* (11), 1032–1036. https://doi.org/10.1038/nphys3805.

(29) Chang, K.; Küster, F.; Miller, B. J.; Ji, J.-R.; Zhang, J.-L.; Sessi, P.; Barraza-Lopez, S.; Parkin, S. S. P. Microscopic Manipulation of Ferroelectric Domains in SnSe Monolayers at Room Temperature. *Nano Lett.* **2020**, *20* (9), 6590–6597. https://doi.org/10.1021/acs.nanolett.0c02357.

(30) Perdew, J. P.; Ruzsinszky, A.; Csonka, G. I.; Vydrov, O. A.; Scuseria, G. E.; Constantin, L. A.; Zhou, X.; Burke, K. Restoring the Density-Gradient Expansion for Exchange in Solids and Surfaces. *Phys. Rev. Lett.* **2008**, *100* (13), 136406. https://doi.org/10.1103/PhysRevLett.100.136406.

(31) Winiarski, M. J.; Samsel-Czekała, M.; Ciechan, A. Strain Effects on the Electronic Structure of the Iron Selenide Superconductor. *EPL Europhys. Lett.* **2012**, *100* (4), 47005. https://doi.org/10.1209/0295-5075/100/47005.

(32) Zhang, G.-X.; Reilly, A. M.; Tkatchenko, A.; Scheffler, M. Performance of Various Density-Functional Approximations for Cohesive Properties of 64 Bulk Solids. *New J. Phys.* **2018**, *20* (6), 063020. https://doi.org/10.1088/1367-2630/aac7f0.

(33) Li, T.; Zhang, X.; Zeng, Z. Factors Affecting the Electron–Phonon Coupling in FeSe under Pressure. *Phys. Chem. Chem. Phys.* **2021**, *23* (44), 25107–25113. https://doi.org/10.1039/D1CP02749B.

(34) Liu, H.; Xue, Y. Van Der Waals Epitaxial Growth and Phase Transition of Layered $FeSe_2$ Nanocrystals. *Adv. Mater.* **2021**, *33* (17), 2008456. https://doi.org/10.1002/adma.202008456.

(35) Kresse, G.; Furthmüller, J. Efficient Iterative Schemes for Ab Initio Total-Energy Calculations Using a Plane-Wave Basis Set. *Phys. Rev. B* **1996**, *54* (16), 11169–11186. https://doi.org/10.1103/PhysRevB.54.11169.

(36) Kresse, G.; Joubert, D. From Ultrasoft Pseudopotentials to the Projector Augmented-Wave Method. *Phys. Rev. B* **1999**, *59* (3), 1758–1775. https://doi.org/10.1103/PhysRevB.59.1758.

(37) Berland, K.; Cooper, V. R.; Lee, K.; Schröder, E.; Thonhauser, T.; Hyldgaard, P.; Lundqvist, B. I. Van Der Waals Forces in Density Functional Theory: A Review of the vdW-DF Method. *Rep. Prog. Phys.* **2015**, *78* (6), 066501. https://doi.org/10.1088/0034-4885/78/6/066501.

(38) Klimeš, J.; Bowler, D. R.; Michaelides, A. Chemical Accuracy for the van Der Waals Density Functional. *J. Phys. Condens. Matter* **2009**, *22* (2), 022201. https://doi.org/10.1088/0953-8984/22/2/022201.

(39) Lee, K.; Murray, É. D.; Kong, L.; Lundqvist, B. I.; Langreth, D. C. Higher-Accuracy van Der Waals Density Functional. *Phys. Rev. B* **2010**, *82* (8), 081101. https://doi.org/10.1103/PhysRevB.82.081101.

(40) Klimeš, J.; Bowler, D. R.; Michaelides, A. Van Der Waals Density Functionals Applied to Solids. *Phys. Rev. B* **2011**, *83* (19), 195131. https://doi.org/10.1103/PhysRevB.83.195131.
(41) Anisimov, V. I.; Gunnarsson, O. Density-Functional Calculation of Effective Coulomb Interactions in Metals. *Phys. Rev. B* **1991**, *43* (10), 7570–7574. https://doi.org/10.1103/PhysRevB.43.7570.
(42) Anisimov, V. I.; Zaanen, J.; Andersen, O. K. Band Theory and Mott Insulators: Hubbard U Instead of Stoner I. *Phys. Rev. B* **1991**, *44* (3), 943–954. https://doi.org/10.1103/PhysRevB.44.943.
(43) Dudarev, S. L.; Botton, G. A.; Savrasov, S. Y.; Humphreys, C. J.; Sutton, A. P. Electron-Energy-Loss Spectra and the Structural Stability of Nickel Oxide: An LSDA+U Study. *Phys. Rev. B* **1998**, *57* (3), 1505–1509. https://doi.org/10.1103/PhysRevB.57.1505.

Figures

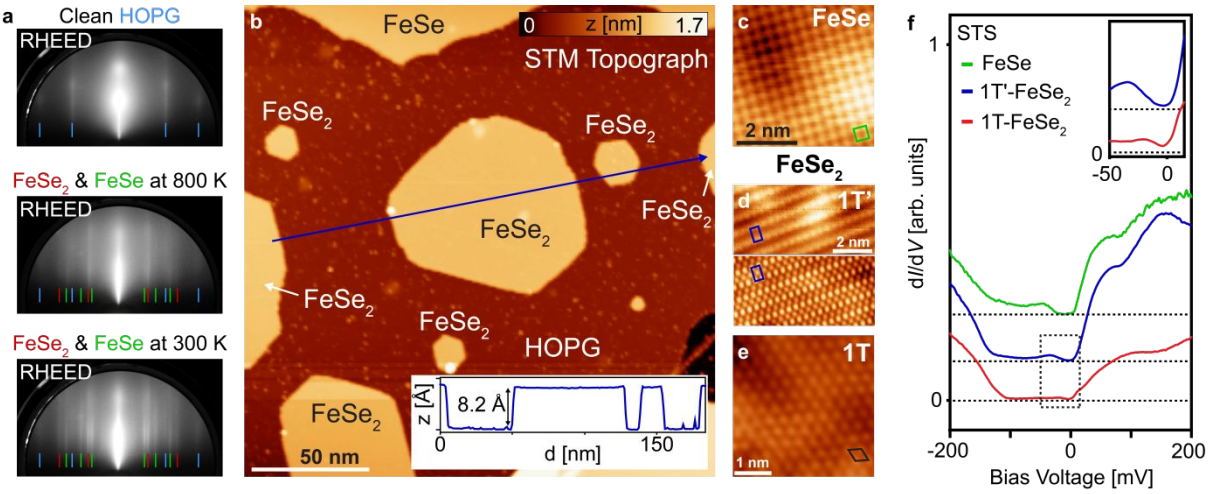

Figure 1 | Growth and structural characterization of $FeSe_2$ monolayers.
(a) RHEED patterns (top to bottom) of clean HOPG (blue), a mixture of monolayer $FeSe_2$ (red) and monolayer FeSe (green) after growth at 800 K, and after cooling down to 300 K. **(b)** Large-scale STM image of typical MBE-grown sample (V_B = -1.0 V, I_T = 10 pA). The inset shows the height profile along the blue line. **(c)** Close-up STM image of an FeSe monolayer with square unit cell (green) (V_B = -1.0 V, I_T = 100 pA). **(d)** Close-up STM image of monolayer 1T'-$FeSe_2$ with rectangular unit cell (blue) (top: V_B = -1.0 V, I_T = 10 pA, bottom: V_B = -1.0 V, I_T = 100 pA). **(e)** Close-up STM image of 1T-$FeSe_2$ monolayer with hexagonal unit cell (black) (V_B = -0.3 V, I_T = 100 pA). **(f)** STS spectra of monolayer FeSe (green), 1T'-$FeSe_2$ (blue), and 1T-$FeSe_2$ (red) (lock-in V_{mod} = 2 mV). The curves have been shifted vertically for easier viewing (dashed lines show dI/dV = 0 for each curve). Inset shows STS spectra in low-bias range for monolayer 1T'-$FeSe_2$ (blue) and 1T-$FeSe_2$ (red) (lock-in V_{mod} = 2 mV). Tip stabilization setpoint for STS: V_B = -0.2 V, I_T = 100 pA.

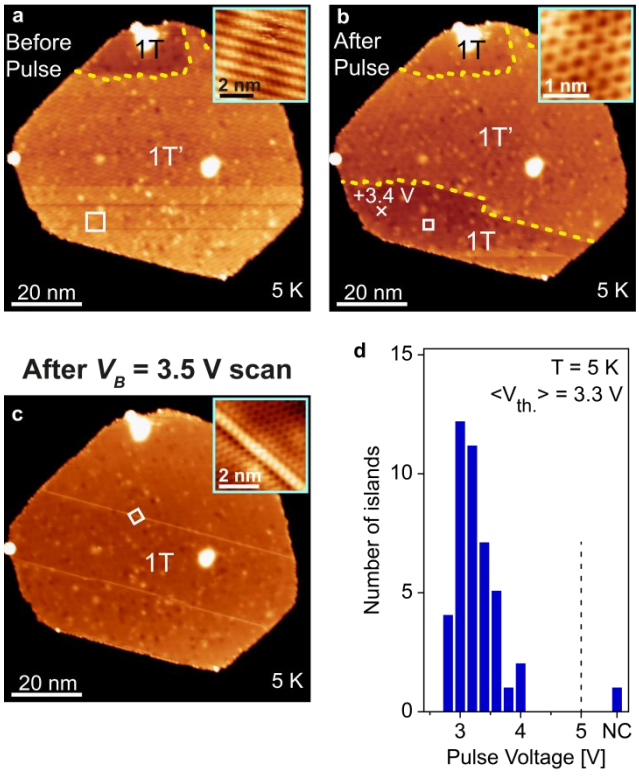

Figure 2 | Electrically-induced structural phase transition in $FeSe_2$ monolayers.

(a) STM image of stripe phase $FeSe_2$ monolayer island before any STM tip manipulation (V_B = -1.0 V, I_T = 10 pA). The boundary between the 1T' stripe phase and the 1T hexagonal phase of the $FeSe_2$ monolayer is indicated by a yellow dashed line. Inset shows a close-up image of the stripe phase (V_B = -1.0 V, I_T = 10 pA). **(b)** Same island shown in **(a)** after a +3.4 V voltage pulse applied at the position indicated by the white "x". Inset shows a close-up image of the hexagonal 1T phase (V_B = -1.0 V, I_T = 10 pA). **(c)** The same island after STM scanning with V_B = +3.5 V and I_T = 10 pA. Inset shows a close-up image of the newly converted 1T hexagonal phase (V_B = -0.3 V, I_T = 100 pA). **(d)** Histogram shows the number of islands converted from stripe phase to hexagonal phase and the minimum voltage pulse required for each conversion. Islands that did not exhibit a phase change from stripe to hexagonal phase for pulses up to 5 V are counted as "non-convertible" (NC).

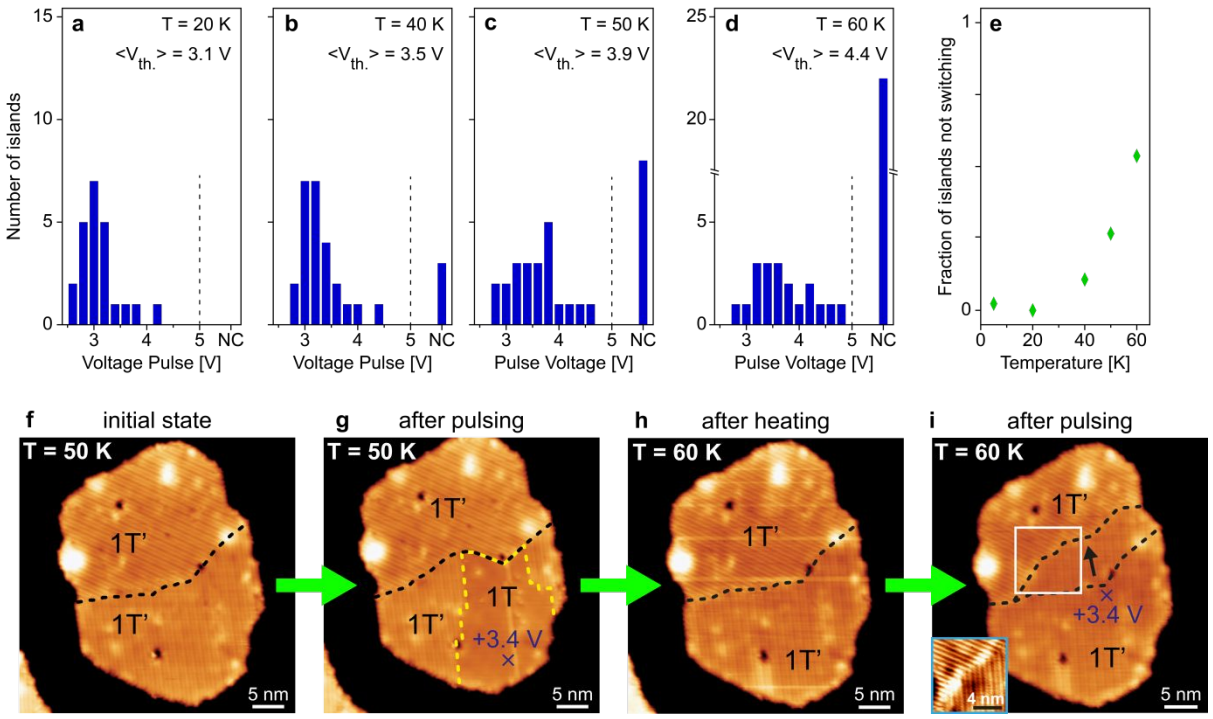

Figure 3 | Thermal reversibility of the structural phase transition in $FeSe_2$ monolayers. Histograms show the number of monolayer islands converted from stripe phase to hexagonal phase (i.e., 1T' to 1T phase) and the minimum voltage pulse required for conversion at **(a)** T = 20 K, **(b)** T = 40 K, **(c)** T = 50 K, and **(d)** T = 60 K. Islands not undergoing phase conversion for pulses up to 5 V are counted as "non-convertible" (NC). **(e)** The temperature dependence of the total fraction of islands counted as non-convertible. STM images of the same monolayer $FeSe_2$ island **(f)** before and **(g)** after a +3.4 V pulse at the position indicated by the blue "x". **(h)** The same island after increasing the sample temperature to 60 K. **(i)** The same island after applying a +3.4 V pulse at the position depicted by the blue "x" (T = 60 K). The boundary between two rotated stripe domains shifts after the voltage pulse as shown by the dashed black lines.

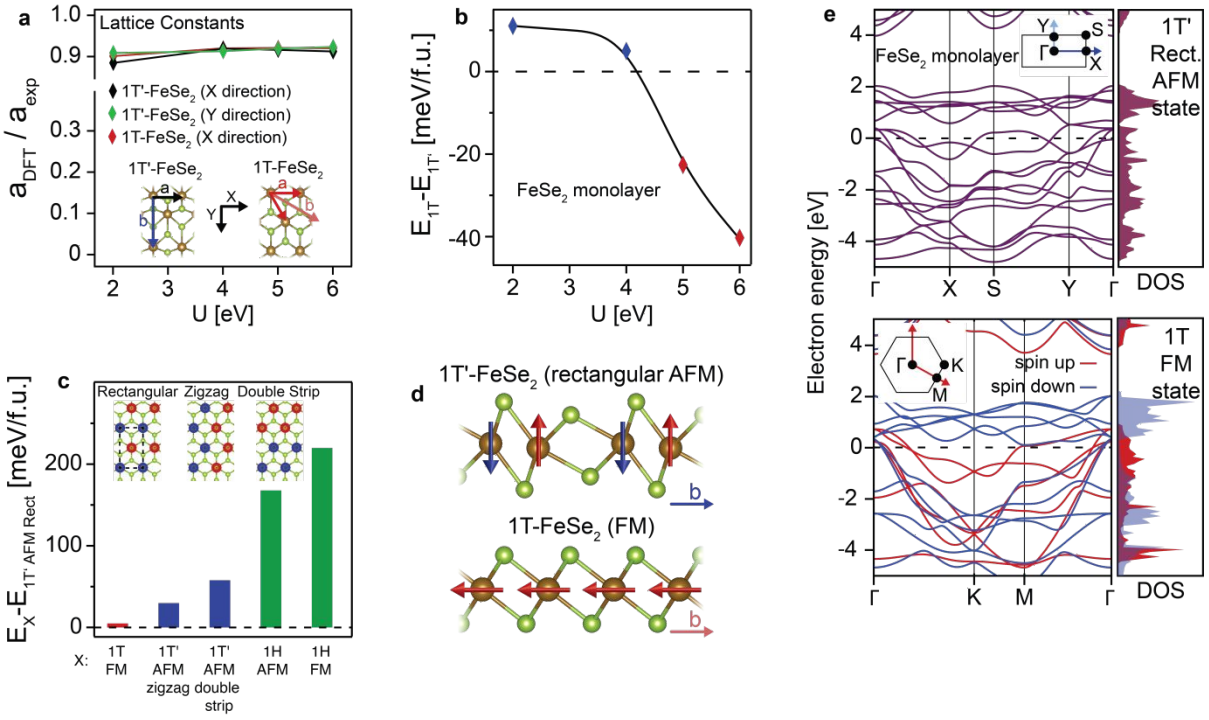

Figure 4 | Calculated energetics of $FeSe_2$ monolayers.

(a) Lattice constants of monolayer 1T'- $FeSe_2$ along X direction (black), monolayer 1T'-$FeSe_2$ along Y direction (green), and monolayer 1T-$FeSe_2$ along X direction (red) derived from DFT+U calculations for different values of U (normalized to the corresponding experimental lattice constants). **(b)** Total energy difference between the monolayer 1T- and 1T'-$FeSe_2$ structures as a function of the Hubbard parameter U in DFT+U calculations. **(c)** Total energy difference between monolayer 1T'-$FeSe_2$ with a rectangular antiferromagnetic (AFM) configuration and different X-$FeSe_2$ polymorphs where X = {1T', 1T, 1H} exhibiting different magnetic ground states (U = 4 eV). The inset shows the three possible calculated 1T' AFM configurations (red means spin up and blue means spin down). **(d)** Magnetic ordering for monolayer 1T'-$FeSe_2$ in the rectangular AFM state and monolayer 1T-$FeSe_2$ in the FM state along the b-direction as defined in **(a)** (the distorted 1T' structure is exaggerated for clarity). **(e)** Band structure and density of states for rectangular AFM monolayer 1T'-$FeSe_2$ (top) and FM monolayer 1T-$FeSe_2$ (bottom).